Check for
updates

Strain Softening of High-Performance Fiber-Reinforced Cementitious Composites in Uniaxial Compression

Seung-Hee Kwon[1], Jung-Soo Lee[1], Kyungtaek Koh[2] and Hyeong-Ki Kim[3*]

Abstract

This study investigates the strain softening behavior of high-performance fiber-reinforced cementitious composites (HPFRCCs) under uniaxial compression. HPFRCC mixtures with different compressive strengths ranged from 120 to 170 MPa were prepared. The measurement method of feedback control on loading rate based transverse displacement was applied. Stress–strain and stress–inelastic displacement curves were plotted and analyzed with the results in the literature. It was found that the post-peak energy absorption of HPFRCC considering inelastic deformation was about 3–7 times higher than conventional concrete. Based on the experimental results in the present work, fitting models on post-peak stress–strain/–displacement curves were considering for different aspect ratios proposed.

Highlights

– Investigated strain softening & snapback of HPFRCC in compression.
– Applied feedback control on loading rate based transverse displacement.
– Formulated stress-strain models for various aspect ratios.
– HPFRCC exhibits higher postpeak energy than conventional concrete.

Keywords High-performance fiber-reinforced cementitious composite (HPFRCC), Compression, Snapback, Size effect, Feedback control, Nonlinear model

*Correspondence:
Hyeong-Ki Kim
hyeongki@chosun.ac.kr
[1] Department of Civil and Environmental Engineering, Myongji University, 116 Myongji-ro, Cheoin-gu, Yongin-si 17058, Republic of Korea
[2] Department of Structural Engineering Research, Korea Institute of Civil Engineering and Building Technology, Goyang-si 10223, South Korea
[3] Department of Architectural Engineering, Chosun University, 309, Pilmun-daero, Dong-gu, Gwangju 61452, Republic of Korea

1 Introduction

In the design and analysis of reinforced concrete structures, properly modeling on the compressive behavior of concrete holds paramount significance. In the case of conventional concrete incorporating coarse aggregates and negligible amount of fiber reinforcement, there are limitations on the designed compressive strength as per the applicable codes. For instance, Eurocode 2 (EN 1992–1) and fib Model Code (MC2010) can be employed for concrete with designed compressive strength less than 90 and 120 MPa, respectively (Hendy et al., 2007; Müller & Boumaaza, 2022). Owing to the brittle behavior exhibited by conventional concrete after reaching the maximum stress, it is not imperative to precisely measure

the post-peak behavior, i.e., the strain–stress relationship after the maximum stress point. Notably, the difference between the strain corresponding to the maximum stress (typically about 0.0030–0.0033) and the ultimate strain (usually about 0.0035–0.0040) for conventional concrete is not significantly large (Minh et al., 2021; Zhang et al., 2012).

On the other hand, high-performance fiber-reinforced cementitious composites (HPFRCCs) or ultrahigh-performance concretes (UHPCs), with a compressive strength ranged from 120 to 220 MPa, have emerged as innovative materials extensively employed for both structural and nonstructural purposes. These materials exhibit markedly distinct mechanical behavior as compared to conventional concrete. Owing to their high volume fraction of fibers (generally exceeding 1 vol.%), they demonstrate strain softening behavior after cracking, rather than brittle. As of now, there is no specific model code catering to concrete with a design standard strength exceeding 120 MPa, especially for mixtures with extremely high toughness like HPFRCCs. Specific design guidelines have been exclusively proposed for HPFRCCs (and UHPCs), such as ultra-high-performance fiber-reinforced concrete (UHPFRC) guidelines in Korea (KCI & F., 2014; Kim et al., 2016), French standard on design for UHPFRC (NF P 18–710 and NF P 18–451) (N.P., 2016; Toutlemonde & F., 2018), design recommendation of UHPFRC in Japan (JSCE & F., 2004; Uchida et al., 2006), and recently, the AASHTO and ACI guide specification for UHPC (Graybeal, 2014; Graybeal & El-Helou, 2019). These guidelines serve to address the unique properties and challenges associated with UHPC in structural applications.

In the majority of codes for structural design, the pre-peak compressive behavior of HPFRCCs was typically modeled with a bilinear curve (Graybeal & El-Helou, 2019). However, these codes often do not account for the post-peak behavior. When considering the substantial post-peak toughness that HPFRCCs gains through fiber reinforcement, it becomes advantage to take into consideration, the strain softening effect for accurately capturing the nonlinear behavior of structures made with this concrete. The conventional bilinear model used to describe the compression behavior of HPFRCCs is inadequate when it comes to simulating the nonlinear behavior of prestressed members or columns that experience high compressive loads (Wei et al., 2019).

Properly modeling the strain softening behavior of this concrete necessitates accurate experimental evaluation. Typically, the relationship between bulk stress and bulk strain is determined by measuring changes in length and loading of concrete specimens under a fixed loading rate. Here, the 'bulk (global) stress and strain' meant that the stress and strain for entire member

of specimen, not considering local stress and strain. However, it is well-known that this post-peak stress–strain relationship is influenced by the structural size and geometry of the concrete member, a phenomenon referred to as the 'size effect' in the crack band theory proposed by (Bažant, 1976; Bažant & Oh, 1983; Pijaudier-Cabot et al., 1988). In general, bulk strain of specimens increases after reaching the peak stress. However, if the length of the specimens is relatively long in relation to the cross-section, i.e., a high aspect ratio, a phenomenon called 'snapback' may occur, where the bulk strain decreases after the peak stress point (Tanabe et al., 2004). Snapback is caused by the recovery of elastic deformation in the noncracked zone of the concrete member after compressive failure (Choi et al., 1996). This snapback phenomenon on rock mechanics was reported by (Hudson et al., 1972) in the 1970s and was actively studied until the 1990s (Bischoff & Perry, 1991; Mier, 1984). Various institutes in the EU, US, and Japan conducted a round-robin test on this topic (RILEM TC 148-SSC) (Mier et al., 1997). However, most of these studies were conducted on structural concrete with normal aggregates and compressive strengths ranging from 30 to 90 MPa (Jansen & Shah, 1997). Even so, most studies on the nonlinear analysis of fiber-reinforced concrete have used the stress–strain models without considering size effects and snapback (Han et al., 2003; Hung & El-Tawil, 2010; Hung & Li, 2013). For HPFRCCs, which has been under investigation since the 2000s, there have been no specific cases studying stress softening considering snapback. The brittleness of the cement matrix in HPFRCCs makes it challenging to accurately measure strain softening, despite the use of fiber reinforcement (Yoo et al., 2016). Further research and experimental studies are required to comprehensively address this aspect and improve the modeling accuracy for HPFRCCs.

In the present work, the strain softening behavior of HPFRCC considering the snapback was studied. A detailed explanation of the compression behavior of the concrete and the concept of the measurement method used was provided in first, aiming to enhance the understanding of the experimental setup. The setup employed for precisely measuring strain softening and the experimental results obtained through this approach was then presented. The pre-peak and post-peak behaviors of HPFRCC in compression were compared with the results reported for conventional concrete in existing literature. Finally, based on the experimental data and analysis, a method to derive the effective strain–stress model of HPFRCC were proposed.
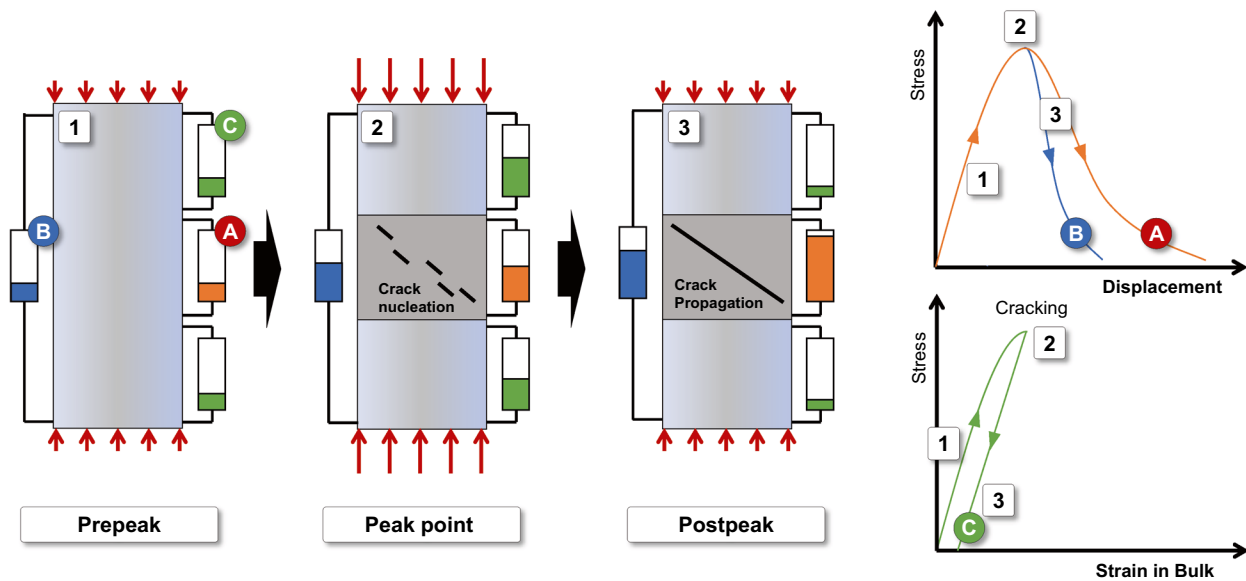
Fig. 1 Localization behavior of concrete in compression ('**A**' and '**C**': local displacements; '**B**': bulk displacement)

2 Behavior in Compression of Concrete and Its Measurement

In this section, a more detailed explanation is provided on the compressive behavior of concrete, which was briefly described earlier. As illustrated in Fig. 1, the compressive behavior of concrete can be divided into two distinct phases: pre-peak and post-peak situations (Jansen & Shah, 1997). To measure the bulk strain, typically, variable displacement transducers (LVDT) are used, which calculate the deformation between the gauge lengths and not the entire specimen. In the pre-peak situation, it can be observed that the strains throughout the concrete member are relatively uniform. However, as the stress approaches the peak point, a number of cracks start to nucleate and eventually propagate, connecting with each other. Subsequently, rapid deformation occurs within the connected crack band (damaged band), while the non-cracked region (uncracked band) exhibits elastic behavior and returns to its original length (Mier, 1984). It is important to note that the actual occurrence of cracks does not precisely happen in one specific location, as depicted in Fig. 1 (Shah et al., 1996). Nevertheless, such a modeling approach is commonly employed to capture the overall behavior of the concrete under compression (Vonk, 1992).

When the length of a concrete specimen is increased, the length of the theoretical damage band does not proportionally increase. This observation was experimentally confirmed by Choi et al. (Choi et al., 1996), who found that the local strain at the post-peak situation varied depending on the position of the specimen, with significant deformations concentrated within a narrow zone. As illustrated in Fig. 2, as the length of the specimen increases, the length of the undamaged band, which undergoes elastic recovery, becomes relatively longer as compared to the damaged band. The measurement of bulk strain at the post-peak situation reflects a more brittle behavior, and in some cases, stress and bulk strain decrease together, leading to the occurrence of snapback. (Tanabe et al., 2004) emphasized the necessity of incorporating a snapback model to analyze the post-peak behavior of reinforced concrete structural members, particularly when calculating the energy absorption of the structures. This underscores the importance of accounting for the snapback effect in accurately predicting the behavior of concrete under high compressive loads, which has implications for designing more resilient and efficient structures in practical engineering applications.

In the past, to obtain the accurate strain softening behavior considering size effect, a number of specimens with varying aspect ratios were prepared and their strain–stress curves were measured (Mier et al., 1997; Rokugo & Koyanagi, 2018; Rokugo et al., 1986). However, the consideration of the size effect using the stress−deformation relationship was later proposed (Jansen & Shah, 1997; Markeset & Hillerborg, 1995). As shown in Fig. 3, the stress−bulk deformation curve was obtained from the specimens and divided into two distinct parts. Firstly, the part corresponding to the undamaged band can be drawn using the peak point and the initial tangent modulus, E_{IT} (A_{pre} in Fig. 3). Secondly, the part corresponding to the damaged band
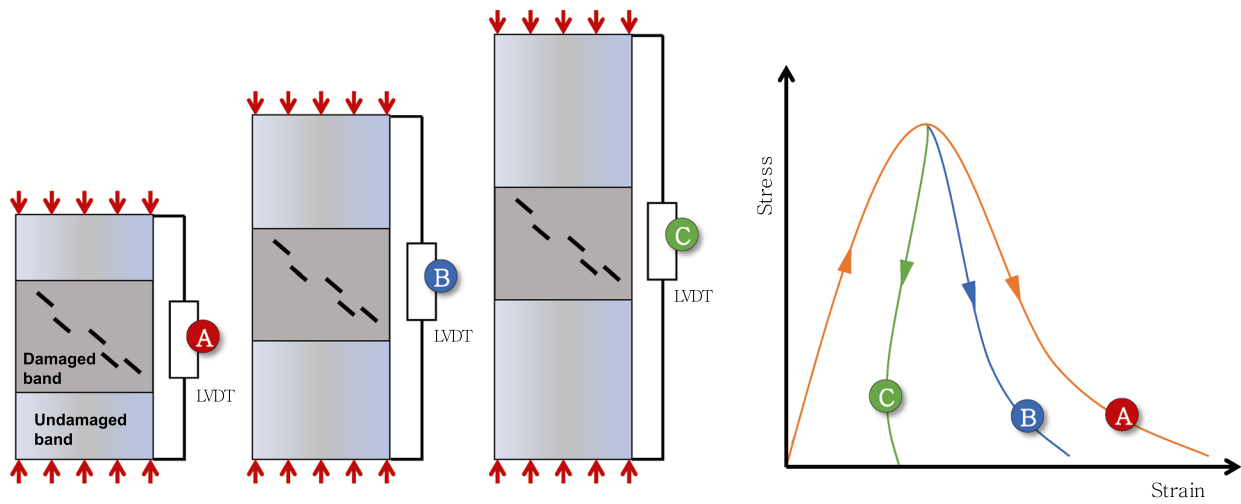
Fig. 2 Geometrical effect on strain–stress relationship of concrete
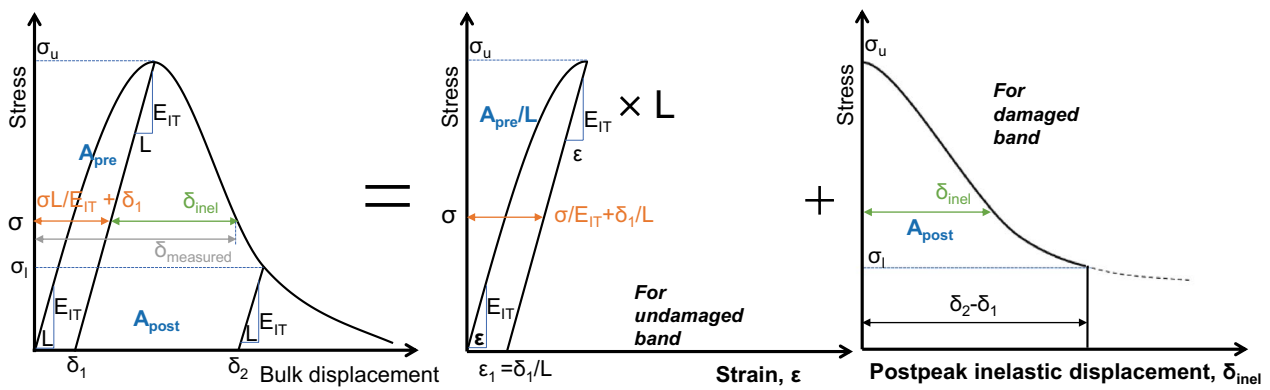
Fig. 3 Stress–displacement curves for concrete in compression considering pre-peak behavior of undamaged band and post-peak softening behavior of damaged band

(A_{post} on the left side of Fig. 3) can be redrawn to reflect the post-peak inelastic deformation, δ_{inel} (A_{post} on the right side of Fig. 3). The δ_{inel} represents a pure deformation of the damaged band, which can be calculated from the bulk deformation and the linear recovery of the undamaged band, as illustrated in Fig. 3.

$$\delta_{inel} = \delta_{measured} - \left(\frac{\sigma L}{E_{IT}} + \delta_1\right) \qquad (1)$$

where $\delta_{measured}$ is bulk deformation of specimen obtained from measurement, σ is the stress level corresponded with the $\delta_{measured}$, L is gauge length, δ_1 is plastic (permanent) deformation after recovery of undamaged band. Here, $\frac{\sigma L}{E_{IT}}$ corresponds the linear deformation at σ for pre-peak curve.

As described earlier, the stress–deformation curve of the undamaged band (A_{pre}) exhibits a linear relationship with the specimen length, whereas the stress-post-peak inelastic deformation curve of the damaged band (A_{post} on the right side of Fig. 3) remains unaffected by the specimen length. This observation allows for the calculation of an effective strain–stress curve that considers both the size effect and the snapback phenomenon. By utilizing these two stress–deformation curves in conjunction with the specimen length, it becomes possible to derive an accurate representation of the mechanical behavior of concrete, accounting for the variations caused by different aspect ratios.

On the other hand, obtaining an accurate stress–deformation curve for HPFRCCs is challenging, especially when dealing with snapback behavior. The issue on measurement method has seldom reported in literature on
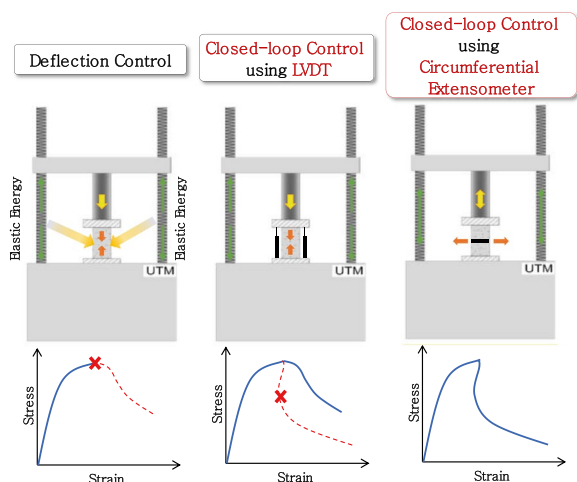
Fig. 4 Effect of measurement method on strain–stress responses of concrete

Fig. 5 Concept of closed-loop control for compression test

HPFRCCs. When stress and strain measurements are taken simply under fixed loading rates, snapback cannot be adequately captured. Moreover, during loading at the pre-peak situation of concrete specimens, elastic energy is stored in the steel frame of the universal testing machine (UTM). Consequently, right after reaching the peak point, the frame rapidly recovers (shrinks), causing the specimen to be suddenly loaded by the frame ('deflection control', left in Fig. 4). The problem is further pronounced for HPFRCCs with very-high strength, as the elastic energy stored in the machine frame becomes substantial, leading to measurements that portray the post-peak curve as more brittle than the actual behavior. To mitigate this measurement error, it is essential to control the loading rate around and after the peak point based on the stress−deformation relationship. When the stress per deformation (the slope of the curve in Fig. 3) decreases around the peak point, the loading rate needs to be controlled and reduced accordingly. This control algorithm is commonly referred to as 'closed loop control,' as it is controlled by the machine's own response, or alternatively, 'feedback control,' as it uses the feedback signal for the elastic response (Fig. 5) (Gettu et al., 1996).

For this control method, both deformations in the load direction (longitudinal displacement) or in the direction perpendicular to the load (transverse displacement) can be used, but the latter gives more accurate and precise results for stress softening than the former. The bulk deformation in the load direction of the specimen, measured by LVDTs or attached strain gauges, is the sum of the deformations in the damaged and undamaged bands (Fujii et al., 1998). Moreover, this value may increase and decrease during the loading history in the post-peak
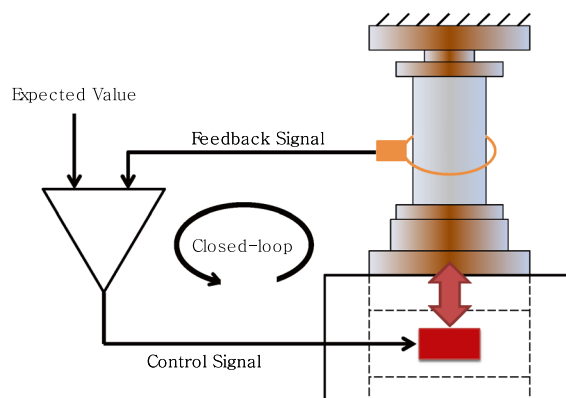
range (snapback). Therefore, using this parameter for feedback control is not ideal (Fujii et al., 1998). When the bulk deformation in the load direction of the specimen was used for loading rate control, although a very slow loading rate is applied around the peak point, the strain of the specimen steadily increases, and snapback cannot be accurately measured ('closed-loop control using LVDT,' middle in Fig. 4).

On the other hand, the lateral deformation gradually and more clearly increases during the loading history in the post-peak range, making it suitable for feedback control. This method has been proposed for rock failure mechanism (Fujii et al., 1998). In this method, the loading rate was controlled using a circumferential extensometer in the perpendicular direction to the load ('closed-loop control using circumferential extensometer,' right in Fig. 4) (Fujii et al., 1998; Shah et al., 1996). In this condition, when the lateral strain exceeds a certain limit, positive and negative loading rates are very sensitively repeated, resulting in a loading−deloading cycle (Shah et al., 1996). This cycle allows for the collection of data on the length recovery of the specimen at the post-peak situation and the corresponding stress decrease (snapback) (Jansen & Shah, 1997).

3 Experimental Details
3.1 Materials and Mix Proportion
The materials and mix proportions used in this study were almost consistent with a series of the previous works (Kang et al., 2016; Kim et al., 2021; Koh et al., 2012, 2013, 2018; Yoo et al., 2018). Type I Portland cement (OPC), ground blast furnace slag (BS), and zirconia silica fume (ZrSF) were employed as binders. Silica powder (SP) and silica sand (S) served as filler and fine aggregate, respectively. In addition, two types of steel fibers with lengths of 19.5 and 16.5 mm (StFr1 and StFr2) were added to the mix. The properties and oxide compositions of OPC, BS,

Table 1 Properties and chemical composition of binders

Material	Surface area (cm²/g)	Specific gravity	Oxide composition (wt.%)								
			CaO	SiO$_2$	Al$_2$O$_3$	Fe$_2$O$_3$	ZrO$_3$	MgO	SO$_3$	Etc	LOI
OPC	3.413	3.15	61.3	21.0	6.4	3.1	–	3.0	2.3	1.5	1.4
BS	4.253	2.89	45.1	32.2	14.2	0.4	–	3.0	3.4	1.7	2.0
ZrSF	15.064	2.50	0.0	94.3	0.4	0.4	3.0	–	–	1.8	0.1

Table 2 Mix proportion

| Mixture name	W/B	W	OPC	BS	ZrSF	SP	S	StFr1	StFr2	AD1	AD2
C120	0.21	210	804	141	60	241	885	78	–	17.8	7.8
C150	0.18	183	823	103	103	247	906	78	39	19.8	7.9
C170	0.18	180	822	–	206	247	905	78	39	18.1	7.9

(Unit: kg/m³; AD1: superplasticizer; AD2: shrinkage reducing agent)

and ZrSF are listed in Table 1. Although silica powder and silica sand shared the same specific gravity of 2.65, their nominal particle sizes (D50) differed, being 4.2 and 520 μm, respectively. To enhance the properties of the mixture, a polycarboxylic acid-based superplasticizer and polyoxyalkylene alkyl ether-based shrinkage reducing agent were also included.

The mix proportions of the various mixtures used in this study are detailed in Table 2. Three different mixtures were prepared with target compressive strengths of 120, 150, and 170 MPa, designated as C120, C150, and C170, respectively. The mixtures C150 and C170 could be classified as UHPC, but C120 was not satisfy this classification (Yoo et al., 2018). It is worth noting that this particular mix proportion has already been commercialized and successfully utilized in bridge structures in practical applications (Kim et al., 2021). The strength of the mixtures was controlled by adjusting the contents of BS, ZrSF, and steel fiber. To ensure workability, the slump flow of the fresh mixtures was maintained at over 650 mm, following the guidelines specified in ASTM C1611.

3.2 Specimen Preparation

A 60 L-capacity Hobart-type mixer was utilized for the mixing process. Initially, the dry components, excluding the steel fiber, were mixed for 10 min at a speed of 90 revolutions per minute (rpm). Subsequently, water and chemical admixtures were added, and the mixture was mixed again for an additional 10 min at a speed of 270 rpm. Finally, the steel fiber was introduced and mixed for 5 more minutes. To ensure uniformity of the mixture, thorough checks were conducted to confirm that all components were adequately mixed. Once this was verified,
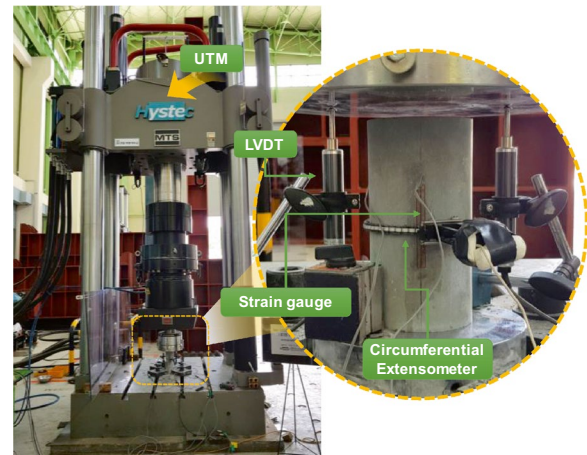
Fig. 6 Experimental setup to evaluate strain softening of HPFRCC

the fresh mixtures were cast into 100×200 mm cylinder molds. The molds were then cured under sealed conditions at a constant temperature of 23 ± 1 °C for the initial 2 days. Subsequently, they were stored in water at the same temperature until the age of 28 days, ensuring a controlled and consistent curing environment for the specimens throughout the testing period.

3.3 Experimental Setup and Data Process

The experimental setup is depicted in Fig. 6. Owing to the requirement for sensitive load control, a 5000 kN class dynamic universal testing machine (UTM) (MTS 311, max. rate of stroke 40 mm/sec, MTS Systems Corporation, US) was employed. For load control, a separate hydraulic power supply (FlexTest SE, 1 ch, 4 stations) was used. Three LVDTs with a measuring
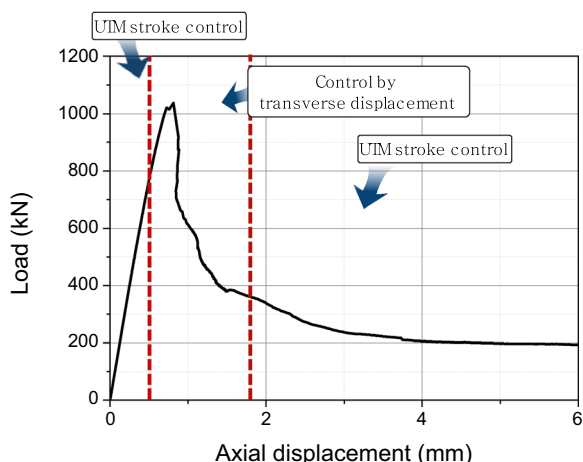
Fig. 7 Loading control scheme

Fig. 8 Modification of raw data

range of 25 mm and an accuracy of 0.025% were installed to measure the longitudinal displacement (load direction) of the specimen, with a gauge length of 200 mm. In addition, a circumferential extensometer with a travel range of 12.5 mm and linearity of 0.25% was installed at the center of the specimen. As illustrated in Fig. 7, the UTM stroke was controlled separately using the load–displacement relationship. During the pre-peak range, a fixed loading rate was applied to reach 80% of the maximum load within 1 min, following the guidelines of ASTM C 39. On the other hand, from approximately 80% of the maximum stress to about 30% of the maximum stress through the peak point, the load was controlled using feedback based on the transverse displacement. For the load control algorithm, the so-called 'partial elastic subtraction method' proposed by (Jansen & Shah, 1997) was implemented. Owing to the presence of a highly sensitive loading–deloading repetition, the actual measured curves resembled fatigue test results, as shown in Fig. 8. To obtain representative data, the raw curves were reorganized into modified curves through initial offset modification and descending point selection. During the descending point selection, points with the largest displacement at each stress level were interpolated and connected after the peak, according to the stress level. To ensure consistency and accuracy in the analysis, 6–8 specimens were tested for each mixture, and data from 3 specimens showing a clear softening behavior were selected and used for further analysis. Note that the data from other specimens did not differ significantly from them. In addition, the photos of the cylinder specimens after finishing the testing, i.e., a loading–deloading repetition, were shown in the Appendix: Fig. 18. A detailed failure pattern can be observed in the figures.
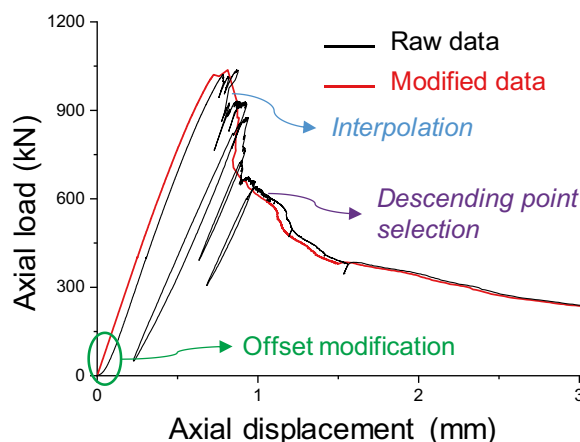
The averaging procedure of load–displacement curves after modification is illustrated in Fig. 9. Initially, 100 datasets were collected for both the ascending and descending parts of the modified curve. The ascending part corresponds to the range from the initial point to the peak point, while the descending part spans from the peak point to the point with an axial displacement of 5 mm. Each dataset was obtained by dividing the load equally into 100 sections for the ascending and descending parts, respectively. Then, the loads and displacements from each section were averaged according to their respective order in the dataset. It is important to note that load–displacement datasets of the same order for different specimens of the same mixture typically yield similar values, which presented in next section.

4 Experimental Results

Fig. 10 illustrates the axial load–bulk displacement curves for the three specimens of each mixture, along with the averaged curve. In some cases, the bulk axial displacement exceeded 5 mm for 200 mm-height specimens (equivalent to 0.025 of bulk strain), but for the sake of clarity, the plot was limited to 4.5 mm (0.0225 of bulk strain) in the figure. It is worth noting that the coefficient of variation (CoV) of load corresponding to the displacement level remained within 30%. Even though there were no specific guidelines or limitations regarding reliability or repeatability, the measurement method employed in this study was considered reliable for capturing the fairly uniform post-peak behavior of the HPFRCCs.

In Fig. 11, the averaged relative stress–bulk deformation curves for the three combinations (C120, C150, and C170 mixtures) are plotted. Notably, it is evident that snapback behavior occurs after the peak point for C150 and C170 mixtures. This observation aligns with the
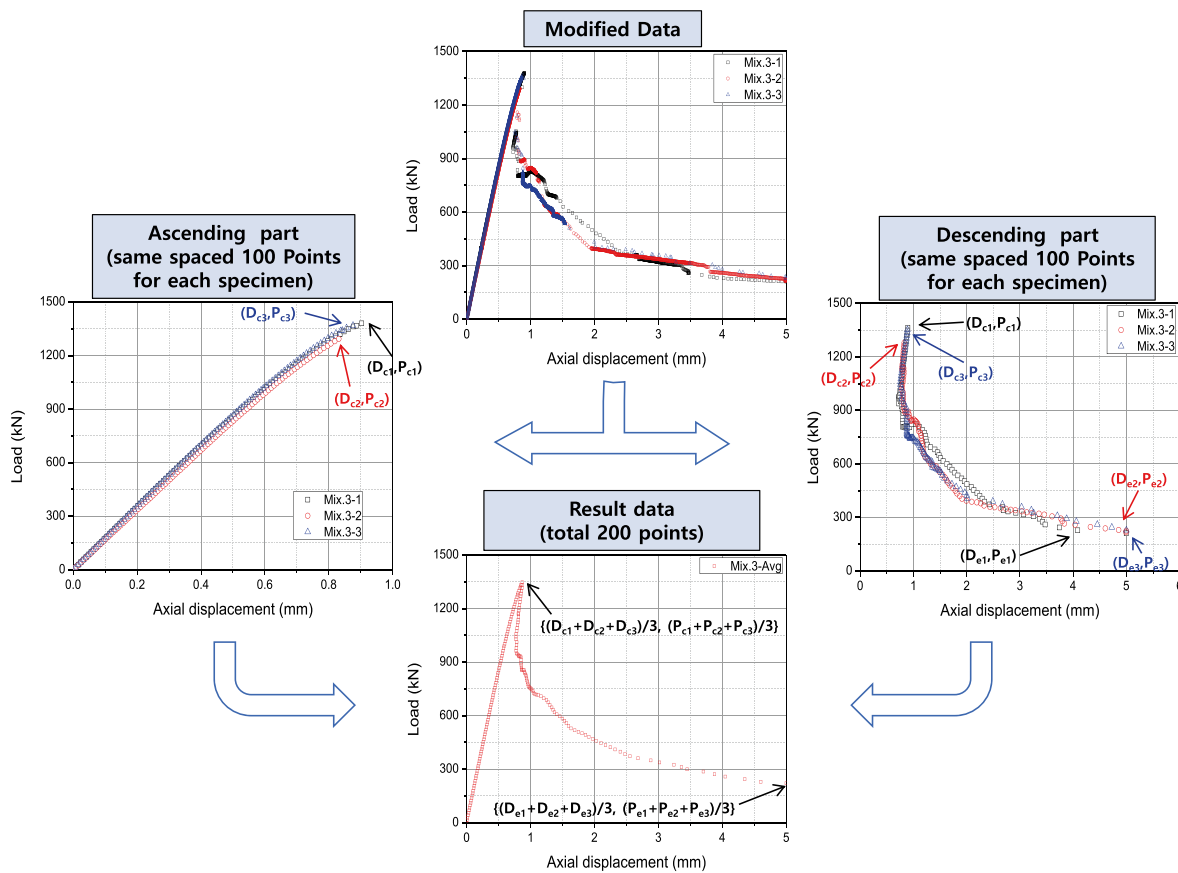
**Fig. 9** Averaging of load–displacement curves

knowledge that high-strength concrete tends to exhibit more brittle behavior in the cement matrix, which may result in snapback. The curves shown in Fig. 11 can be further divided into stress–strain curves and stress–inelastic displacement curves for the damaged and undamaged zones, respectively.

In Fig. 12, the pre-peak strain–stress curves for the undamaged band of the three mixtures (C120, C150, and C170) are presented. The elastic recovery lines were calculated based on the peak point and initial tangent elastic modulus. It was observed that the proportional limit and strain at maximum stress for all mixtures were approximately 0.003 and 0.0040–0.0045, respectively. Comparatively, conventional concrete without fiber reinforcement typically exhibits a proportional limit and strain at maximum stress of around 0.0015–0.002 and 0.002–0.003, respectively (Samani & Attard, 2014). Hence, the incorporation of steel fiber reinforcement led to an increase in energy absorption within the pre-peak region. The ε_1 value for the mixtures ranged within 0.0004–0.0006. The CoV for compressive

strength σ_u and ε_1 for all mixtures were within 3% and 8%, respectively. However, it was challenging to find references on the specific values of ε_1, which might be due to limited existing data or variations in test methods and materials. Overall, the findings indicate that the steel fiber reinforcement significantly improved the energy absorption capacity of the pre-peak curves under compression. In future research, the impact of fiber content and direction on the energy absorption capacity of UHPC will be assessed.

Fig. 13 displays the post-peak stress–inelastic deformation curves for the damaged band of the three types of mixtures (C120, C150, and C170). As in the previous studies (Jansen & Shah, 1997; Rokugo et al., 1986), the stress limit to calculate post-peak energy, shown in Fig. 4, was set at 33.3% of the relative stress ($\sigma_l/\sigma_u = 1/3$). The corresponding stress values and associated inelastic deformations were presented in Fig. 13. However, it should be noted that the deviation of the post-peak curves was larger than that of the pre-peak curves. Consequently, the post-peak inelastic deformation

Kwon *et al. Int J Concr Struct Mater*   (2024) 18:17

Page 9 of 15
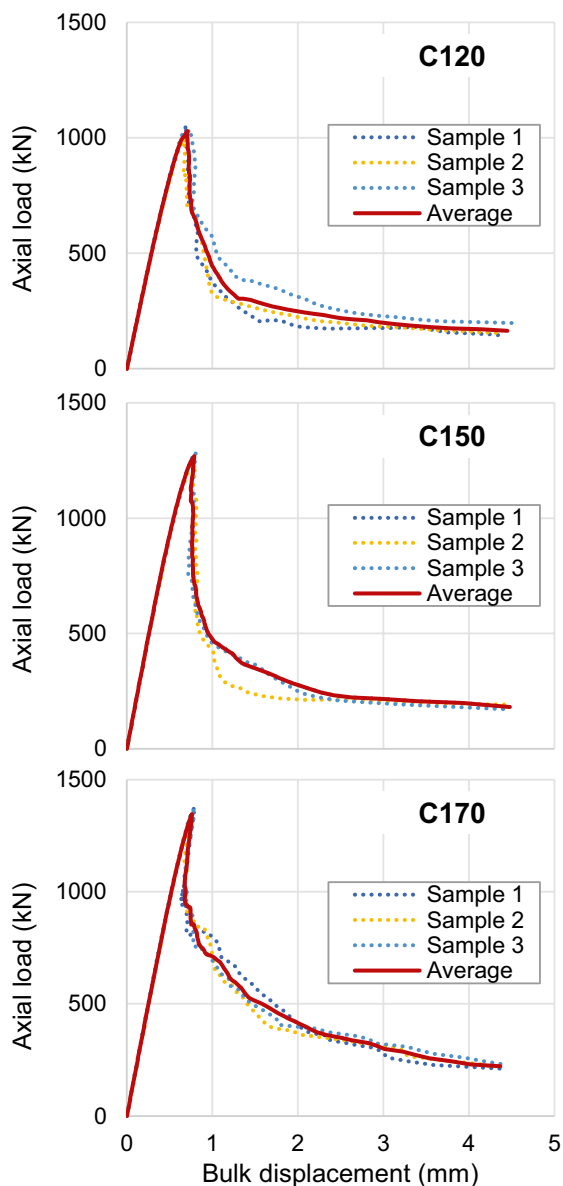
Fig. 10 Axial load−bulk displacement curves of UHPC in uniaxial loading

corresponding to the stress σ exhibited a significant difference, ranging from 25 to 50% of the average value.

5 Discussion

Figs. 14 and 15 present the pre-peak and post-peak energies of the HPFRCCs per unit area of the cross-section, respectively. As explained in Fig. 4, the energies per unit area of the cross-section in Figs. 14 and 15 are obtained by calculating the areas under the curves in Figs. 12 and 13, respectively. For the post-peak curves,

stress−deformation curves below 33.3% of the relative stress were omitted during the calculation. The results from the present study were compared with those from the previous research on conventional normal- and high-strength concrete (Jansen & Shah, 1997; Rokugo et al., 1986). Although there was an attempt to include more results from other studies, few approaches similar to the present study were found, limiting the extent of comparison. The findings revealed that both pre-peak and post-peak energies of the HPFRCC in the present work were higher than those of conventional concrete without fiber reinforcement. In Fig. 14, it can be observed that the pre-peak energy showed a linear correlation with the gauge length of the specimen. As explained in Figs. 2 and 3, the pre-peak stress−strain curve was considered to be equivalent regardless of the geometry of the concrete specimen, allowing the pre-peak energy to be calculated by multiplying the area covered by the stress−strain curve with the length of the specimen. However, it is important to note that the prepeak energy does not necessarily appear to be strictly proportional to the compressive strength of the concrete, as indicated by the results of both conventional concrete and HPFRCC in the present work. This suggests that factors beyond compressive strength may influence the pre-peak energy, such as the energy absorption of aggregates during compression or discrepancies in the elastic properties between aggregates and the cement paste, which can affect the nonlinearity of the concrete behavior.

As mentioned earlier, the post-peak energy of the HPFRCC was found to be constant regardless of the length of the specimen. In addition, it was intriguing to observe that the post-peak energies of conventional concrete exhibited similar values within a range of approximately 20 ± 5 N/mm (Jansen & Shah, 1997; Rokugo et al., 1986). In contrast, the post-peak energy of HPFRCC was notably higher, ranging from 3–7 times higher than that of conventional concrete without fiber reinforcement. This significant difference in post-peak energy between HPFRCC and conventional concrete highlights the importance of considering strain softening in compression during the nonlinear analysis of HPFRCC members. If the post-peak energy of HPFRCC may calculated with lower relative stress limitation, this value became increase due to higher ductility of the mixtures.

Fig. 16 presents a comparison of the post-peak relative stress−inelastic displacement curves between HPFRCC and conventional concrete from literature. To obtain the curves for conventional concrete, relevant figures in the literature were digitized using the 'Digitize' tool in the OriginPro software, and the data points were plotted
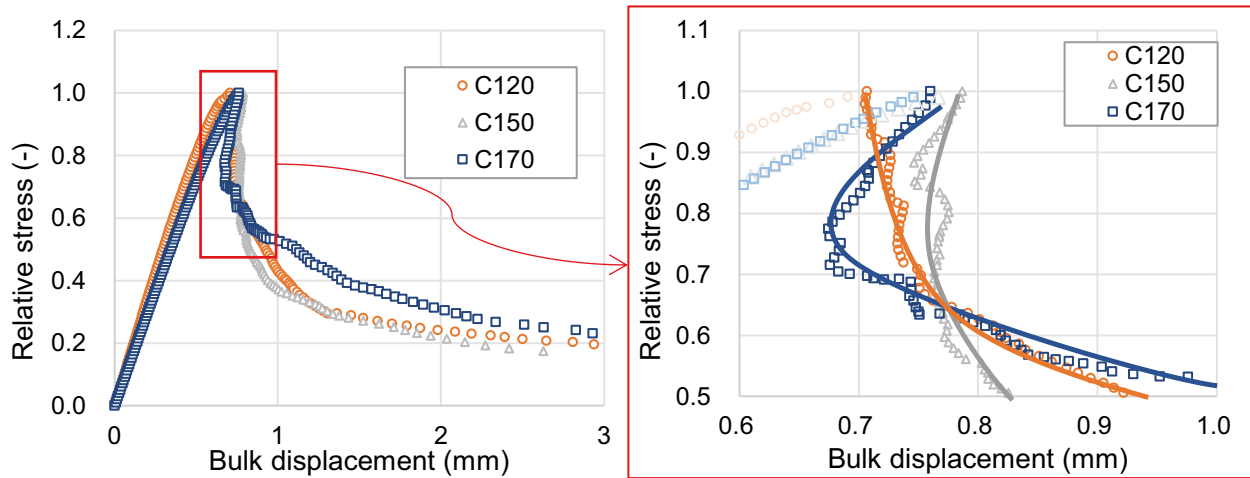
Fig. 11 Snapback of UHPC in relative stress−bulk displacement curves (dot: measured; line: fitted)

in the figure. Despite some deviations in the post-peak stress−inelastic displacement curves, a fitting model corresponding to the minimum values of relative stress could be derived as follows:

$$\sigma_{m-post} = \sigma_u[(1-a)\exp(b\delta_{inel}) + a] \qquad (2)$$

where, σ_{m-post} is a post-peak stress corresponding to inelastic displacement δ_{inel} (MPa), and a (−) and b (1/mm) are the fitting parameters. For Fig. 16, the compressive strength measured from the experiment adopted to the values of σ_u. However, for the design, the required strength could be applied for the σ_u.

When considering the strain softening behavior and safety concerns for concrete under compression, adopting the exponential fitting model corresponding to the minimum value of stress, rather than an averaged one, is deemed reasonable. The fitting parameters extracted from Fig. 16 have been listed in Table 3. As previously mentioned, these parameters may vary depending on various factors such as the mix proportion used in the concrete and fiber orientation. It was interesting that the parameters for HPFRCC in the present work in Fig. 16 was similar to those for conventional high-strength concrete. However, due to the fiber reinforcement, the allowable ranges of inelastic displacement for HPFRCC was much larger than those for the conventional concrete.

It is worth noting that other types of fitting models for post-peak relative stress−inelastic displacement curves, such as Hillerborg's bilinear model (Roesler et al., 2007) which generally used for post-peak behavior in tensile

of concrete, could also be considered for the curves in Fig. 16. However, in the present work, only the exponential fitting model corresponding to the minimum value of stress was used and presented.

Combining the pre-peak stress−strain curve from Fig. 12 and the post-peak stress−inelastic displacement model given in Eq. 2 allows for the calculation of post-peak bulk displacement and bulk strain using the following equation:

$$\delta_{m-post} = \delta_{inel} + \left(\frac{\sigma_{m-post}L}{E_{IT}} + \delta_1\right)$$

$$\epsilon_{m-post} = \frac{\delta_{m-post}}{L} \qquad (3)$$

where δ_{m-post} is a modeled axial post-peak bulk displacement considering the length of concrete element, and ϵ_{m-post} is modeled effective strain corresponding δ_{m-post}.

Through the application of these equations, it becomes possible to calculate the pre- and post-peak stress−strain/−displacement models of concrete for various aspect ratios. Fig. 17 displays the stress−displacement and stress−strain models of HPFRCC with different aspect ratios. As observed in the figure, the post-peak model was derived through fitting based on the minimum value of stress from the experimental results presented in Fig. 16, resulting in the identification of snapback behavior in all cases illustrated in Fig. 17. As expected, the
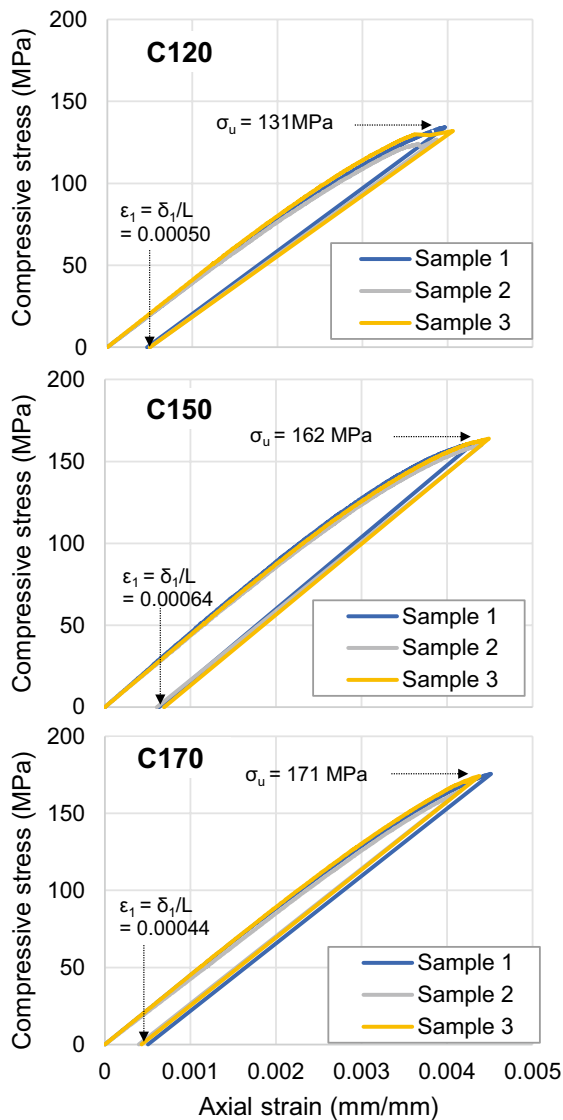
**Fig. 12** Strain−stress curves for undamaged band of UHPC
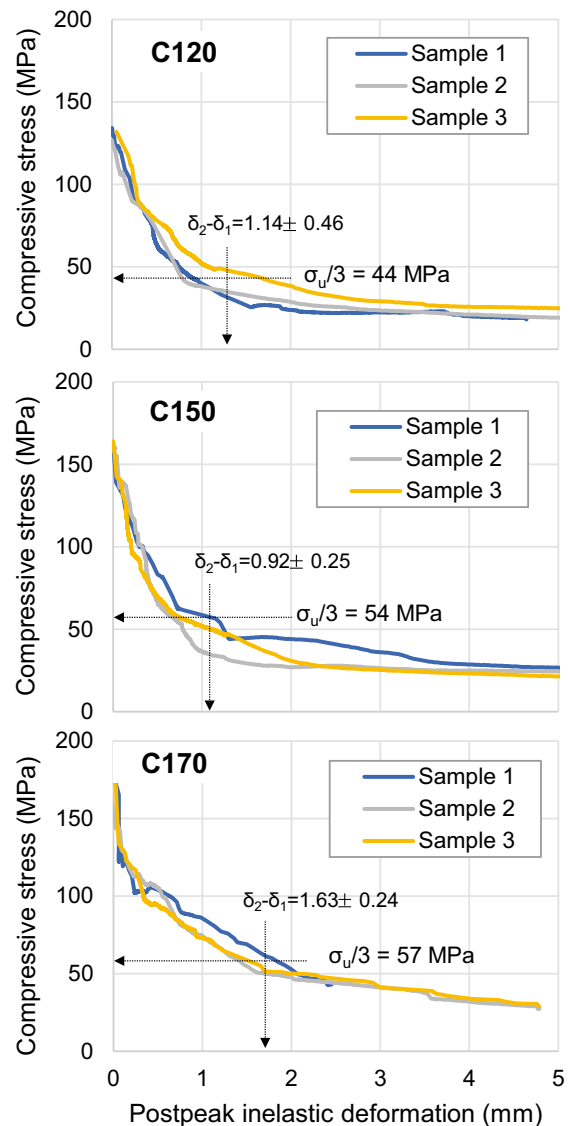
Fig. 13 Post-peak inelastic deformation−stress curves for damaged band of UHPC

snapback becomes more pronounced as the aspect ratio increases, indicating that longer undamaged bands relative to the overall length of the concrete members lead to a clearer snapback effect. The stress−strain curves in Fig. 17 could be applied in nonlinear structural analysis in the future work.

In addition, this study has a limitation in that the size effect on the cross section of the specimen was not considered. Moreover, other factors, including the loading rate, specimen geometry, fiber volume fraction, and direction, should also be considered in the stress−displacement and strain models.

6 Conclusion

Through the present work, strain softening of high-performance fiber-reinforced cementitious composites in uniaxial compression considering snapback was studied. A detailed explanation of the compression behavior of the concrete and the concept of the measurement method used was provided in first, aiming to enhance the understanding of the experimental setup. A sensitive and precise measurement method to evaluate the load−displacement relationship of HPFRCC under uniaxial
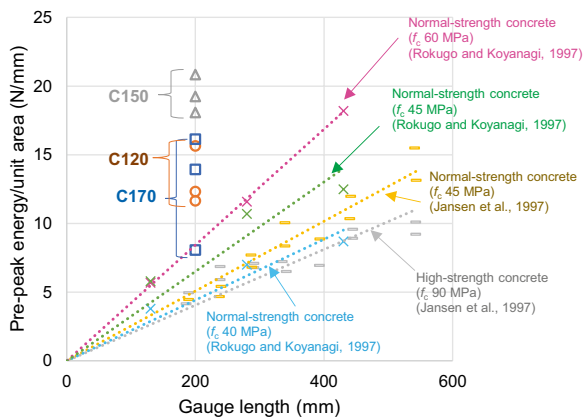
Fig. 14 Pre-peak energies per unit area of cross section for HPFRCC and conventional concrete (Jansen & Shah, 1997; Rokugo et al., 1986)
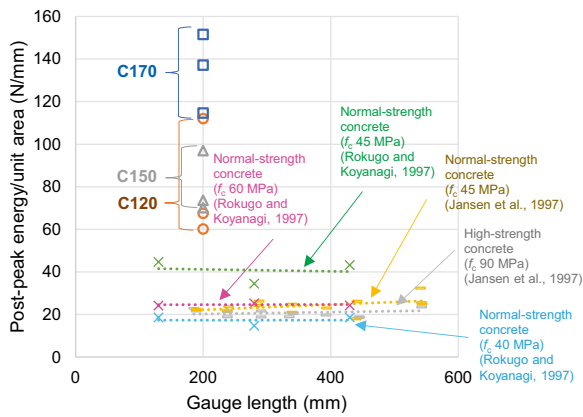
Fig. 15 Post-peak energies per unit area of cross section for HPFRCC and conventional concrete (Jansen & Shah, 1997; Rokugo et al., 1986)

compression was applied. The HPFRCC exhibit the compressive strength ranged from 120 to 170 MPa were prepared, and their pre-peak and post-peak behaviors under comparison was analyzed with the results in the literature. The conclusions drawn from a series of case studies are as follows:

i. The proportional limit and strain at maximum stress for all mixtures were approximately 0.003 and 0.0040–0.0045, respectively, which was much higher than conventional concrete without fiber reinforcement. Therefore, the steel fiber reinforcement increased the energy absorption of pre-peak curves.
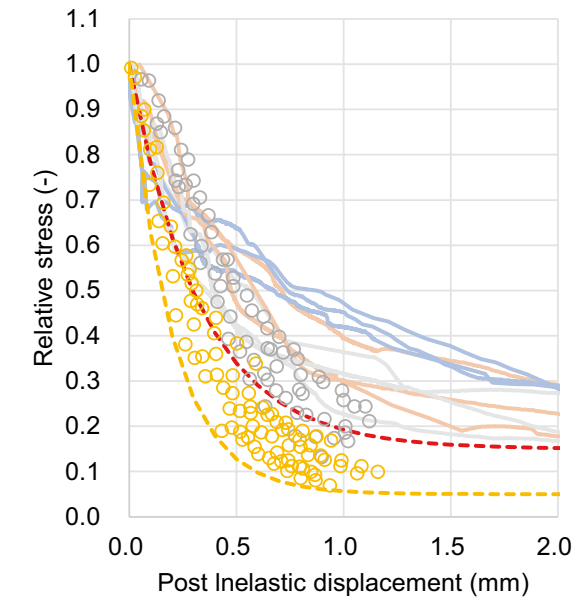

Fig. 16 Comparison of post-inelastic displacement–relative stress curves for HPFRCC and other concrete in the literature

Table 3 Parameters for the minimum fitting on Eq. 2

Concrete type	a (-)	b (1/mm)	Maximum value of allowable δ_{inel} (mm)
HPFRCC (C120, C150, C170)	0.15	− 3	4
High-strength concrete (f_c 90 MPa) (Jansen & Shah, 1997)	0.15	− 3	0.6
Normal-strength concrete (f_c 45 MPa) (Jansen & Shah, 1997)	0.05	− 5	0.6

ii. The pre-peak stress–strain curve was considered to be equivalent regardless of the geometry of the concrete specimen, allowing the pre-peak energy to be calculated by multiplying the area covered by the stress–strain curve with the length of the specimen. However, it is important to note that the pre-peak energy does not necessarily appear to be

Kwon *et al. Int J Concr Struct Mater* (2024) 18:17

Page 13 of 15
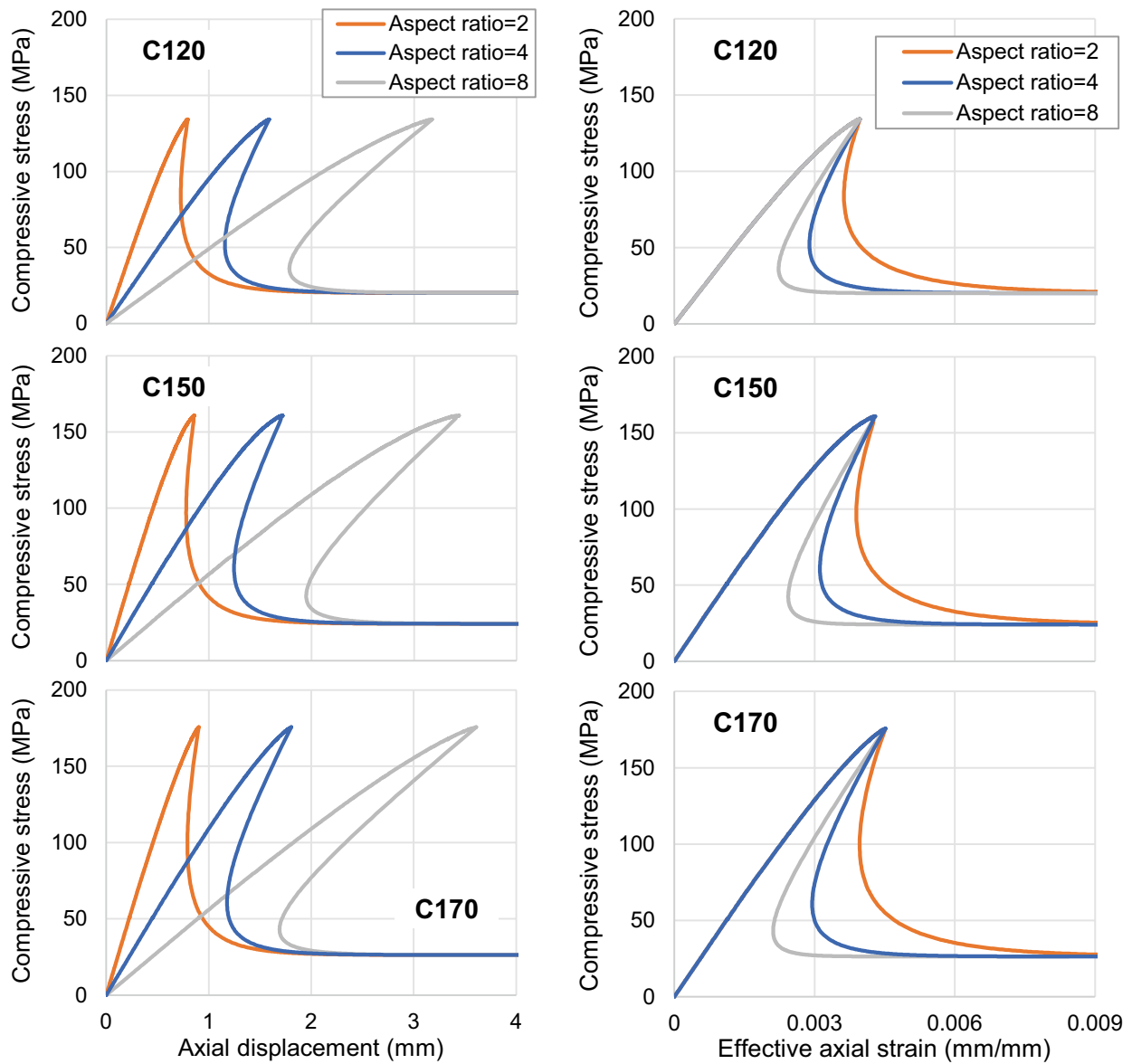
Fig. 17 Calculated stress–displacement (left) and –strain (right) models of HPFRCC with various aspect ratios (pre-peak curves were adopted from experiment, while post-peak curves were from model in Eq. 3)

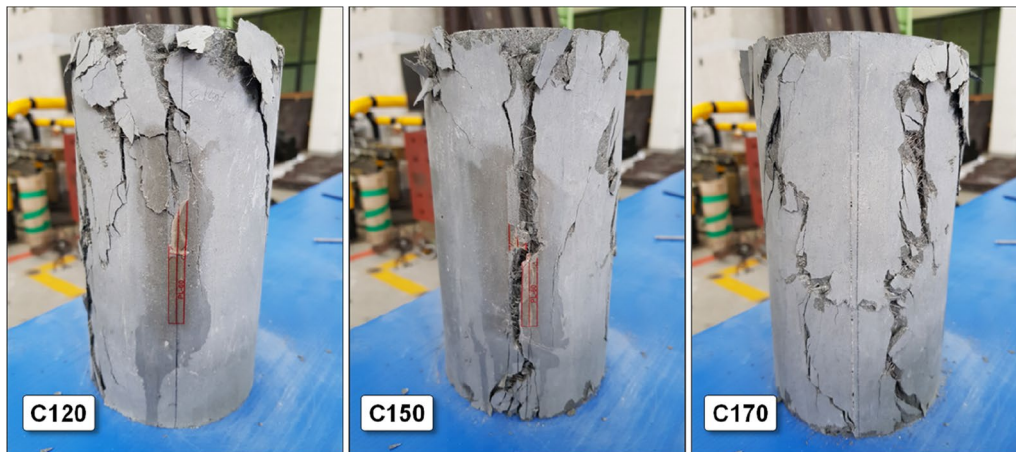strictly proportional to the compressive strength of the concrete.

iii. Despite some deviations in the post-peak stress– inelastic displacement curves, a fitting model cor-responding to the minimum values of relative stress was proposed. This model can be used for nonlinear analysis of HPFRCC with various aspect ratios.

Appendix

See Fig. 18

Fig. 18 Concrete specimens after loading−deloading repetition

Author contribution
Seung-Hee KWON : Conceptualization, Methodology, Validation, Writing - Original Draft; Jung-Soo LEE: Data Curation, Resources, Writing - Original Draft; Kyungtaek Koh : Supervision, Project administration, Funding acquisition; Hyeong-Ki KIM : Investigation, Formal analysis, Writing - Original Draft, Writing - Review & Editing, Visualization.

Availability of data and materials
All the datasets associated with this study are available from the corresponding author upon request.

Declarations

Ethics approval and consent to participate
All authors of the manuscript confirm the ethics approval and consent to participate following the Journal's policies.

Consent for publication
All authors of the manuscript agree on the publication of this work in the International Journal of Concrete Structures and Materials.

Competing interests
The authors declare no competing interests.

References

Bažant, Z. P. (1976). Instability, ductility, and size effect in strain-softening concrete. *Journal of the Engineering Mechanics Division, 102*(2), 331–344.

Bažant, Z. P., & Oh, B. H. (1983). Crack band theory for fracture of concrete. *Matériaux Et Construction, 16*, 155–177.

Bischoff, P., & Perry, S. (1991). Compressive behaviour of concrete at high strain rates. *Materials and Structures, 24*, 425–450.

Choi, S., Thienel, K.-C., & Shah, S. P. (1996). Strain softening of concrete in compression under different end constraints. *Magazine of Concrete Research, 48*(175), 103–115.

Fujii, Y., Kiyama, T., Ishijima, Y., & Kodama, J. (1998). Examination of a rock failure criterion based on circumferential tensile strain. *Pure and Applied Geophysics, 152*, 551–577.

Gettu, R., Mobasher, B., Carmona, S., & Jansen, D. C. (1996). Testing of concrete under closed-loop control. *Advanced Cement Based Materials, 3*(2), 54–71.

Graybeal BA, RG El-Helou. Development of an AASHTO Guide Specification for UHPC. In: International Interactive Symposium on Ultra-High Performance Concrete. 2019. Iowa State University Digital Press.

Graybeal, B. (2014). *Design and construction of field-cast UHPC connections*. United States: Federal Highway Administration.

Han, T.-S., Feenstra, P. H., & Billington, S. L. (2003). Simulation of highly ductile fiber-reinforced cement-based composite components under cyclic loading. *Structural Journal, 100*(6), 749–757.

Hendy, C. R., & Smith, D. A. (2007). *Designers' guide to EN 1992–2: eurocode 2: design of concrete structures: part 2: concrete bridges*. Westminster: Thomas Telford.

Hudson, J. A., Crouch, S. L., & Fairhurst, C. (1972). Soft, stiff and servo-controlled testing machines: a review with reference to rock failure. *Engineering Geology, 6*(3), 155–189.

Hung, C.-C., & El-Tawil, S. (2010). Hybrid rotating/fixed-crack model for high-performance fiber-reinforced cementitious composites. *ACI Materials Journal*. https://doi.org/10.1435/51664043

Hung, C.-C., & Li, S.-H. (2013). Three-dimensional model for analysis of high performance fiber reinforced cement-based composites. *Composites Part B: Engineering, 45*(1), 1441–1447.

Jansen, D. C., & Shah, S. P. (1997). Effect of length on compressive strain softening of concrete. *Journal of Engineering Mechanics, 123*(1), 25–35.

JSCE, F. (2004). *Recommendations for design and construction of ultra-high strength fiber reinforced concrete structures (Draft)*. Japan: Japan Society of Civil Engineers Tokyo.

Kang, S.-T., Choi, J.-I., Koh, K.-T., Lee, K. S., & Lee, B. Y. (2016). Hybrid effects of steel fiber and microfiber on the tensile behavior of ultra-high performance concrete. *Composite Structures, 145*, 37–42.

KCI, F. (2014). *Design guidelines for K-UHPC*. Korea: Korea Concrete Institute Seoul.

Kim, B. S., Joh, C., Koh, G. T., Park, J., Kwon, K., & Park, S. Y. (2016). KICT's application of UHPC to the first UHPC cable stayed roadway bridge. In International Interactive Symposium on Ultra-High Performance Concrete (Vol. 1, No. 1). Iowa State University Digital Press. https://doi.org/10.21838/uhpc.2016.97https://www.iastatedigitalpress.com/uhpc/article/id/9597/

Kim, H., Moon, B., Hu, X., Lee, H., Ryu, G.-S., Koh, K.-T., Joh, C., Kim, B.-S., & Keierleber, B. (2021). Construction and performance monitoring of innovative ultra-high-performance concrete bridge. *Infrastructures, 6*(9), 121.

Koh, K.-T., G.S. Ryu, J.-J. Park, K. An, S. Kim and S.-T. Kang. Effects of the composing materials on the rheological and mechanical properties of ultra-high performance concrete (UHPC). In: Proceedings of the RILEM-fib-AFGC International Symposium on UHPFRC, Marseille, France. 2013.

Koh, K. T., Park, J. J., Kang, S. T., & Ryu, G. S. (2012). Influence of the type of silica fume on the rheological and mechanical properties of ultra-high performance concrete. *Key Engineering Materials, 488*, 274–277.

Koh, K. T., Park, S. H., Ryu, G. S., An, G. H., & Kim, B. S. (2018). Effect of the type of silica fume and filler on mechanical properties of ultra high performance concrete. *Key Engineering Materials, 774*, 349–354.

Markeset, G., & Hillerborg, A. (1995). Softening of concrete in compression—localization and size effects. *Cement and Concrete Research, 25*(4), 702–708.

Minh, H.-L., Khatir, S., Wahab, M. A., & Cuong-Le, T. (2021). A concrete damage plasticity model for predicting the effects of compressive high-strength concrete under static and dynamic loads. *Journal of Building Engineering, 44*, 103239.

Müller, H. S., & Boumaaza, M. (2022). Modeling concrete properties: new approaches in MC2020. *Structural Concrete*. https://doi.org/10.1002/suco.202201231

NP. (2016). *National addition to Eurocode 2-design of concrete structures: specific rules for ultra-high performance fiber-reinforced concrete*. Saint-Denis Cedex: Association Française de Normalisation (AFNOR).

Pijaudier-Cabot, G., Bažant, Z. P., & Tabbara, M. (1988). Comparison of various models for strain-softening. *Engineering Computations, 5*(2), 141–150.

Roesler, J., Paulino, G. H., Park, K., & Gaedicke, C. (2007). Concrete fracture prediction using bilinear softening. *Cement and Concrete Composites, 29*(4), 300–312.

Rokugo K, S Ohno, W Koyanagi Automatical measuring system of load-displacement curves including post-failure region of concrete specimens. Fracture toughness and fracture energy of concrete, 1986: p. 403–412.

Rokugo, K., & Koyanagi, W. (2018). Role of compressive fracture energy of concrete on the failure behavior of reinforced concrete beams. *Applications of fracture mechanics to reinforced concrete* (pp. 437–464). CRC Press.

Samani, A. K., & Attard, M. M. (2014). Lateral strain model for concrete under compression. *ACI Structural Journal, 111*(2), 441–451.

Shah, S. P., Choi, S., & Jansen, D. C. (1996). Strain softening of concrete in compression. *Proc Fract Mech Concr Struct, 3*, 1827–1841.

Tanabe, T.-A., Itoh, A., & Ueda, N. (2004). Snapback failure analysis for large scale concrete structures and its application to shear capacity study of columns. *Journal of Advanced Concrete Technology, 2*(3), 275–288.

Toutlemonde, F. (2018). Completion of the French Standards for UHPC: Highlights of the Standard for Execution of UHPFRC Structures NF P 18–451. In ACI Committee 239 Ultra-High Performance Concrete (pp. 10-p). https://uhpc.com.vn/wp-content/uploads/2018/09/NF-P-18-710-UHPC.pdf

Uchida Y, J Niwa, Y Tanaka, M Katagiri, G Fischer, V Li. Recommendations for design and construction of ultra high strength fibre reinforced concrete structures. Concrete committee of Japan Society of Civil Engineers (JSCE), 2006: p. 345–351.

Van Mier, J., Shah, S., Arnaud, M., Balayssac, J., Bascoul, A., Choi, S., Dasenbrock, D., Ferrara, G., French, C., & Gobbi, M. (1997). Strain-softening of concrete in uniaxial compression: report of the round robin test carried out by RILEM TC 148-SSC. *Materials and Structures, 30*, 195–209.

Van Mier JGM. Strain-softening of concrete under multiaxial loading conditions. 1984.

Vonk RA. Softening of concrete loaded in compression. 1992.

Wei, J., Li, J., & Wu, C. (2019). An experimental and numerical study of reinforced conventional concrete and ultra-high performance concrete columns under lateral impact loads. *Engineering Structures, 201*, 109822.

Yoo, D.-Y., Banthia, N., Kang, S.-T., & Yoon, Y.-S. (2016). Size effect in ultra-high-performance concrete beams. *Engineering Fracture Mechanics, 157*, 86–106.

Yoo, D.-Y., Kim, M.-J., Kim, S., Ryu, G.-S., & Koh, K.-T. (2018). Effects of mix proportion and curing condition on shrinkage behavior of HPFRCCs with silica fume and blast furnace slag. *Construction and Building Materials, 166*, 241–256.

Zhang, X., Ruiz, G., Rena, C. Y., Poveda, E., & Porras, R. (2012). Rate effect on the mechanical properties of eight types of high-strength concrete and comparison with FIB MC2010. *Construction and Building Materials, 30*, 301–308.

Publisher's Note
Springer Nature remains neutral with regard to jurisdictional claims in published maps and institutional affiliations.

Seung-Hee Kwon   Professor, Department of Civil and Environmental Engineering, Myongji University

Jung-Soo Lee   Research Professor, Department of Civil and Environmental Engineering, Myongji University

Kyungtaek Koh   Senior Researcher, Department of Structural Engineering Research, Korea Institute of Civil Engineering and Building Technology

Hyeong-Ki Kim   Professor, Department of Architectural Engineering, Chosun University